



# YFeO<sub>3</sub> Photocathodes for Hydrogen Evolution

María Isabel Díez-García<sup>a</sup>, Verónica Celorrio<sup>b</sup>, Laura Calvillo<sup>c</sup>, Devendra Tiwari<sup>b</sup>, Roberto Gómez<sup>a</sup>, David J. Fermín<sup>b,\*</sup>

<sup>a</sup> Departament de Química Física i Institut Universitari d'Electroquímica, Universitat d'Alacant, Apartat 99, E-03080 Alacant, Spain

<sup>b</sup> School of Chemistry, University of Bristol, Cantocks Close, BS8 1TS, Bristol, UK

<sup>c</sup> Dipartimento di Scienze Chimiche, Università di Padova, Via Marzolo 1, 35131 Padova, Italy

## ARTICLE INFO

### Article history:

Received 24 March 2017

Received in revised form 26 May 2017

Accepted 5 June 2017

Available online 9 June 2017

### Keywords:

YFeO<sub>3</sub>  
perovskite  
nanoparticles  
photocurrent  
band tails

## ABSTRACT

The behavior of YFeO<sub>3</sub> thin-film electrodes under illumination is investigated for the first time. YFeO<sub>3</sub> thin films on F-doped SnO<sub>2</sub> (FTO) electrodes were prepared by two different methods (A) deposition of nanoparticles synthesized by the so-called ionic liquid route at 1000° C followed by sintering at 400° C and (B) spin coating of a sol-gel precursor followed by a heat treatment at 640° C. Method A provides highly texture films with exquisite orthorhombic phase purity and a direct band gap transition at 2.45 eV. On the other hand, method B results in very compact and amorphous films. XPS confirmed a Fe<sup>3+</sup> oxidation state in both films, with a surface composition ratio of 70:30 Y:Fe. Both materials exhibit cathodic photocurrent responses arising from hydrogen evolution in alkaline solutions with an onset potential of 1.05 V vs. RHE. The complex behavior of the photoresponses is rationalized in terms of recombination losses, band edge energy tails and hindered transport across the oxide thin film.

© 2017 The Authors. Published by Elsevier Ltd. This is an open access article under the CC BY license (<http://creativecommons.org/licenses/by/4.0/>).

## 1. Introduction

Photoelectrochemical (PEC) water splitting can potentially offer a viable and scalable approach for solar energy conversion into fuels. This approach is commonly seen in competition with integrating photovoltaic modules to water electrolyzers (PC-EC); two mature technologies which can deliver solar-to-hydrogen (STH) efficiencies in the range of 10–12%. Techno-economic analysis have shown that PEC can be a viable technology only if STH efficiencies in excess of 15% can be achieved [1,2]. Given the severe constraints associated with the dynamics of multi-electron transfer reactions such as oxygen evolution, requiring high energy carriers, STH efficiencies above 12% cannot be realistically achieved with a single absorber material [1]. Consequently, tandem devices featuring dimensionally stable photoanodes and photocathodes represent the key challenge in this field. Therefore, it is crucial to extend current research activities beyond conventional oxide photoanodes (such as TiO<sub>2</sub>, ZnO, Fe<sub>2</sub>O<sub>3</sub>, BiVO<sub>4</sub> and WO<sub>3</sub>) into materials capable of generating hydrogen under illumination [3–6].

A number of materials have been reported as photocathodes for hydrogen evolution, including Si [7,8], Cu<sub>2</sub>O [9,10], GaP [11], and

InGaN [12]. In these studies, the stability of the semiconductor surface under operation conditions is crucially important. A number of ternary oxides have been investigated as photocathodes, including spinels (CaFe<sub>2</sub>O<sub>4</sub> [13–15], CuFe<sub>2</sub>O<sub>4</sub> [16]), delafossites (CuFeO<sub>2</sub> [17], CuCrO<sub>2</sub> [18]) and perovskites (LaFeO<sub>3</sub> [19–21]). Ferrite perovskites are a particularly interesting class of materials featuring band gap values in the range of 2.3–2.4 eV. Recently, Celorrio et al. investigated the photoelectrochemical properties of phase-pure LaFeO<sub>3</sub> nanoparticles sintered on FTO electrodes [19], while compact thin films have been fabricated by pulsed laser deposition [20] and sol-gel methods [21].

In this work, we describe the synthesis and properties of YFeO<sub>3</sub> as a photocathode for hydrogen evolution reaction under alkaline conditions. Despite several reports about YFeO<sub>3</sub> as a photocatalyst for water remediation [22–25] and photochemical H<sub>2</sub> production [26], very little is known about key properties such as band edge energy positions and charge transport properties. We shall investigate two different synthesis routes, leading to sintered nanostructured (NP-Films) and compact films (C-Films) supported on FTO. The rationale for investigating these two different morphologies is to assess the effect of grain boundaries and material disorder on the dynamics of minority charge carrier transfer, hole collection and carrier recombination. Despite the different level of crystallinity obtained from both methods, the films exhibit cathodic photocurrents associated with hydrogen evolution at potentials as positive as 1.05 V vs RHE under visible

\* Corresponding author.

E-mail address: [David.Fermin@bristol.ac.uk](mailto:David.Fermin@bristol.ac.uk) (D.J. Fermín).

light illumination. However, incident-photon-to-current efficiency are rather modest, suggesting that carrier collection is limited to those generated near the FTO/YFeO<sub>3</sub> boundary. The materials are characterized by X-ray diffraction, X-ray photoelectron spectroscopy, diffuse reflectance and electron microscopy.

## 2. Experimental Section

### 2.1. YFeO<sub>3</sub> nanoparticle thin film electrode (NP)

YFeO<sub>3</sub> nanoparticles were synthesized following the ionic liquid protocol [19]. 1 mL of an aqueous solution of 0.05 M of Y(NO<sub>3</sub>)<sub>3</sub>·6H<sub>2</sub>O (99.8%, Sigma-Aldrich) and 0.05 M of Fe(NO<sub>3</sub>)<sub>3</sub>·9H<sub>2</sub>O (99.95%, Sigma) was added to a vial containing 1 mL of 1-ethyl-3-methylimidazolium acetate (97%, Sigma Aldrich). The solution was dehydrated at 80 °C for 3 h and 100 mg of cellulose was added before calcination at 1000 °C for 2 h. This method yields phase-pure YFeO<sub>3</sub> nanoparticles.

Approximately 1 μm-thick films were fabricated via the doctor blade method over FTO (F:SnO<sub>2</sub>) conductive glass. First, 100 μg of the YFeO<sub>3</sub> powder was suspended in 100 μL of water and sonicated for 15 min in an ultrasonic bath. Acetylacetone (Sigma Aldrich) and Triton 100X (Fisher Scientific) were added in order to obtain a homogeneous and viscous paste. Finally, the paste was spread over the FTO and sintered at 400 °C for 1 h in air.

### 2.2. YFeO<sub>3</sub> compact thin film electrode (C)

The synthesis is based in a sol-gel method using citric acid as a chelating agent. Y(NO<sub>3</sub>)<sub>3</sub>·6H<sub>2</sub>O (0.3 M) and Fe(NO<sub>3</sub>)<sub>3</sub>·9H<sub>2</sub>O (0.3 M) were dissolved in water and the solution was stirred for 1 h. Citric acid monohydrated (99.8%, Fisher) was added to a concentration of 0.6 M and stirred for 20 h. A gel was obtained by adding 30 μL/mL of acetylacetone and 30 μL/mL of Triton 100X. A portion of 25 μL of the sol-gel was spin coated over the FTO substrate at 3000 rpm for 20 s and calcined at 400 °C for 1 h. This procedure was repeated twice (2-layers), followed by heating at 640 °C for 2 h, leading to approximately 80 nm-thick films. The same heating procedure was followed in a crucible to generate powder samples for XRD analysis.

### 2.3. Instrumentation

X-ray diffraction (XRD) was recorded using a Bruker AXS D8 Advance diffractometer with a  $\theta$ - $\theta$  configuration, using a Cu K $\alpha$  radiation ( $\lambda = 0.154$  nm). Transmission electron microscopy (TEM) and high resolution TEM were carried out on a JEOL JEM-1400Plus and a JEOL JEM-2010 microscopes, respectively. Field emission scanning electron microscopy (FE-SEM) images were obtained by a ZEISS Merlin VP Compact microscope. Energy-dispersive X-ray (EDX) analysis was performed with a SEM instrument JEOL SEM 5600 LV. A Shimadzu UV-2401PC spectrophotometer equipped with an integrating sphere coated with BaSO<sub>4</sub> was used to measure UV-visible diffuse reflectance spectra. Core level photoemission spectra was collected in normal emission at room temperature with a K-Alpha Thermo-Scientific X-ray Photoelectron Spectrometer (XPS) using an Al K $\alpha$  X-ray source. Electrochemical measurements were performed in a three-electrode cell equipped with a fused silica window using a computer-controlled Ivium Compact-Stat equipment. A Ag/AgCl/KCl(3 M) electrode was used as a reference, while a platinum wire was used as a counter electrode. The electrolyte solution used in all experiment was 0.1 M NaOH purged with high purity Ar. Measurements under illumination were carried out using a LED with a narrow emission centered at 404 nm LED (Thorlabs), driven by a waveform generator (Stanford

Research Systems). Photon flux was measured employing a calibrated silicon photodiode (Newport Corporation).

## 3. Results and Discussion

Fig. 1A contrasts the XRD patterns of YFeO<sub>3</sub> obtained from ionic liquid and sol-gel routes. Full profile Rietveld refinement on XRD pattern of the sample resulted from ionic liquid route is performed, confirming the formation of YFeO<sub>3</sub> in orthorhombic phase (*Pnma*) with lattice parameters  $a = 5.5936$  Å,  $b = 7.6023$  Å and  $c = 5.2796$  Å. The unit cell (inset Fig. 1A) is composed of Fe<sup>3+</sup> centred octahedra, with oxygen atoms occupying non-symmetric axial and equatorial positions. Fe atom is found to be off-centred leading to two different bond lengths between Fe and equatorial oxygen (O<sub>eq</sub>) atoms: 196.35 and 203.29 pm, while Fe to axial O (O<sub>ax</sub>) bond lengths are same and equal to 198.89 pm. Similarly, the bond angles formed between O<sub>eq</sub> and Fe and the O<sub>ax</sub>-Fe-O<sub>eq</sub> angles deviate from the ideal 90° by up to 2.72° and 11.62°, respectively. Stabilization of FeO<sub>6</sub> polyhedra is brought on the expense of acute distortion of Y-O bonds. Overall bulk composition is slightly metal deficient, promoting p-type conductivity. No other peaks due to secondary phases composing tetrahedrally coordinated Fe, such as in Y<sub>3</sub>Fe<sub>5</sub>O<sub>12</sub> garnet frequently formed during the synthesis of YFeO<sub>3</sub>, are observed within the measurement limit [27,28]. Structure parameters ascertained from the refinement can be found in supplementary information.

The C-film shows no clear diffraction peaks, indicating a lack of crystallinity (Fig. 1A, bottom panel). The key difference in the synthesis method is the temperature used for promoting the orthorhombic YFeO<sub>3</sub> phase. Zhang et al. [24] reported the crystallization of YFeO<sub>3</sub> powder from 700 °C using a sol-gel route with citric acid as chelating agent, which is slightly above the temperature limit set by the stability of the substrate

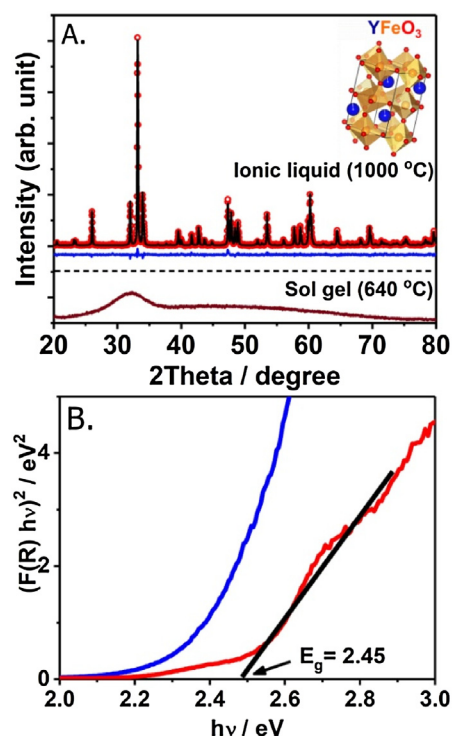


**Fig. 1.** (A) Powder XRD patterns of YFeO<sub>3</sub> particles obtained by the ionic liquid method at 1000 °C and sol-gel route at 640 °C. (B) Tauc plot, direct transition, corresponding to NP (red line) and C (blue line) films. A band gap of 2.45 eV was estimated for the NP film. (For interpretation of the references to colour in this figure legend, the reader is referred to the web version of this article.)

(approximately 640 °C). The crystallization temperature reflects the enthalpy of formation of the perovskite phase which is influenced by the nature of the A and B site [29,30]. For instance, phase pure  $\text{LaFeO}_3$  synthesized by the same ionic-liquid approach can be achieved at 900 °C, while  $\text{LaMnO}_3$  can be obtained at 700 °C [31].

Fig. 1B shows Tauc plots corresponding to the NP and C-films obtained by operating the Kubelka-Munk function ( $F(R)$ ) on the reflectance spectra. The spectra (Supporting Information, Fig. S1) show absorption edges at 600 and 650 nm for the NP and C films, respectively. The Tauc plot representation shows a direct band gap transition for the NP-film at 2.45 eV, which is in close agreement with previous studies in the literature [23,32]. On the other hand, C-films do not show a clearly defined linear region which is consistent with the amorphous nature of the material. This behaviour can be explained in terms of potential fluctuations of the band edge energies, which lead to the so-called Urbach tails [33,34]. We shall come back to this point further below.

SEM images in Fig. 2A and B contrast the smooth nature of the C-films against the nanoscale corrugated NP-films. TEM images in Fig. 2C show that the particles obtained after calcination at 1000 °C exhibit a size distribution between 100 and 200 nm. The lattice fringes displayed in the high-resolution TEM image (Fig. 2D) correspond to a d-spacing of 0.27 nm associated with the {121} plane, which is consistent with the most prominent feature in XRD (Fig. 1A). The structural features of the TEM images further demonstrate the high crystallinity and phase purity of the particles obtained by the ionic-liquid method.

Both films are characterized by homogeneous Y and Fe distributions as shown in Fig. 3. EDX mapping does not show regions in which a single element is segregated, i.e. the Y/Fe is constant throughout the surface. This experimental evidence is particularly important in the case of the C-films, in which XRD and

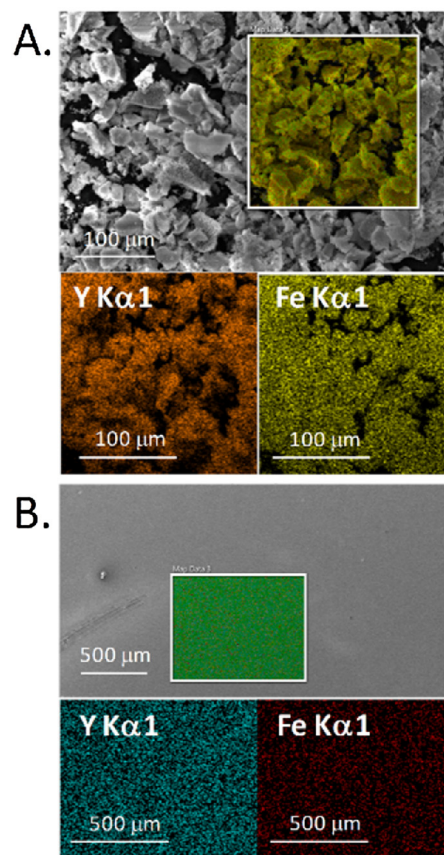


Fig. 3. SEM micrographs (upper images) and the corresponding elemental mapping of Y and Fe for NP (A) and C (B) thin films.

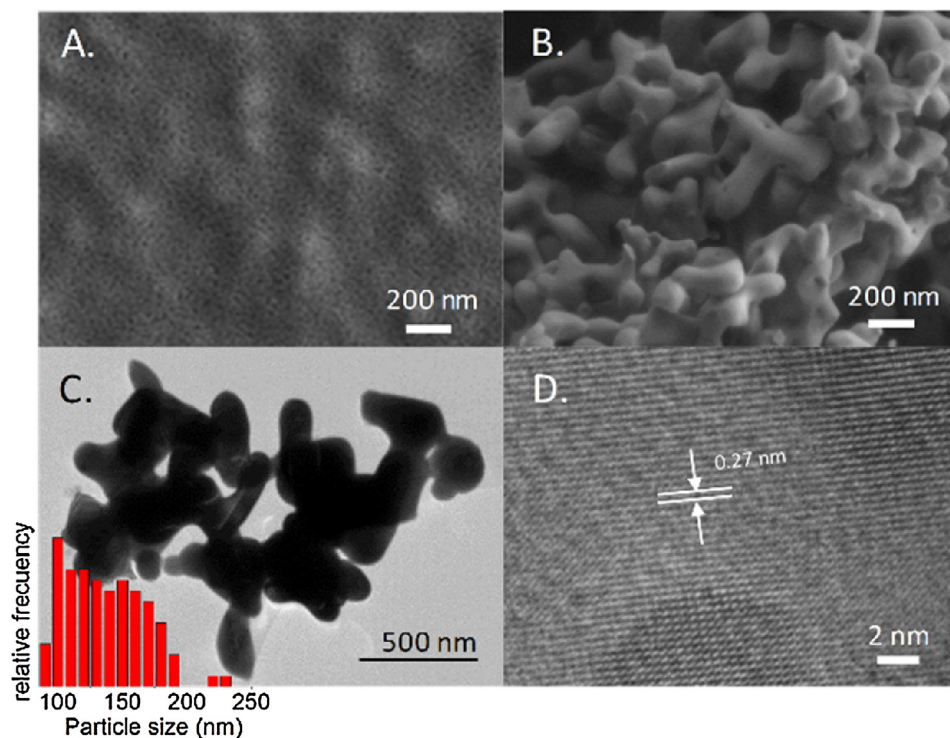
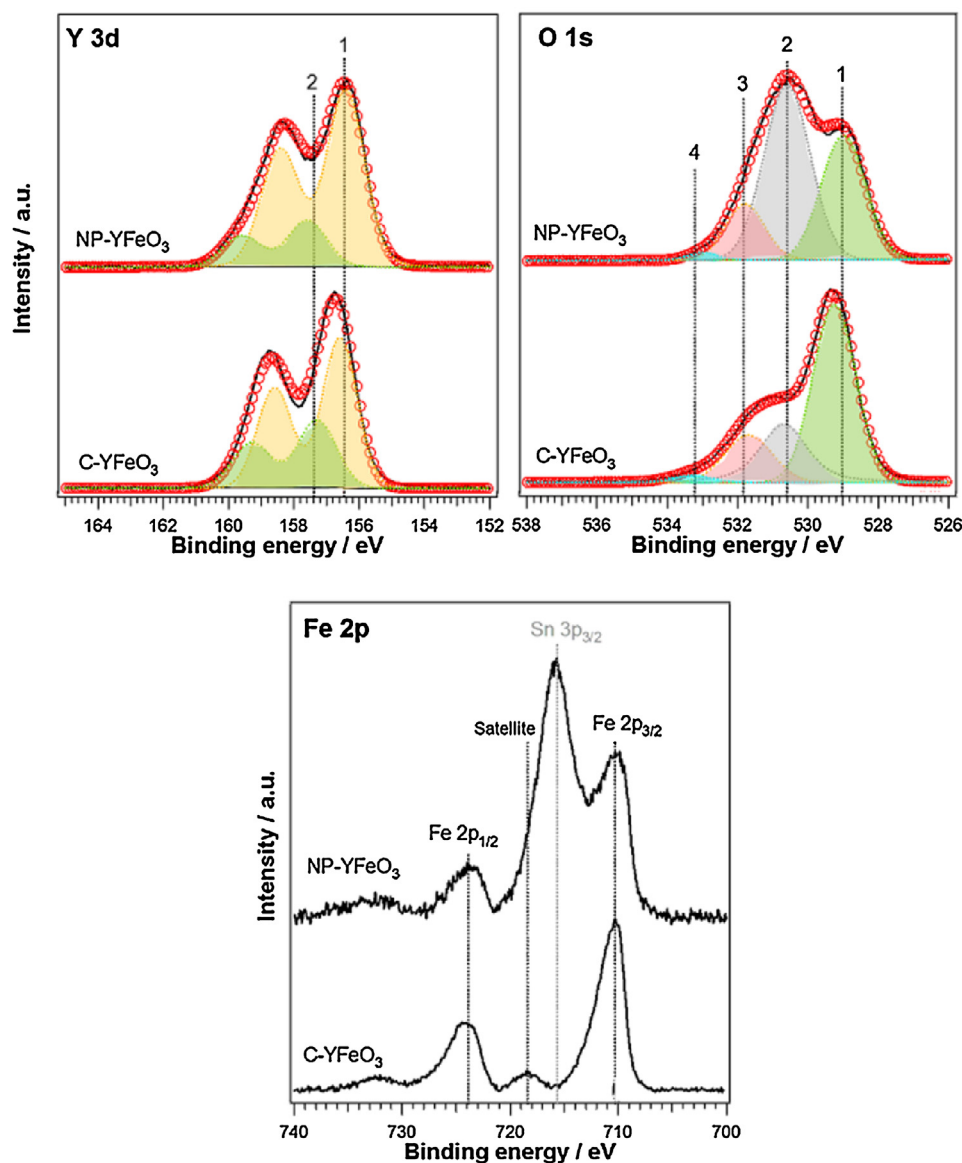


Fig. 2. FE-SEM images for (A) C-film (B) the NP-film. (C) TEM micrograph of the nanoparticles obtained by the ionic-liquid method at 1000 °C. Inset: Particle size distribution determined from TEM images (over 100 nanoparticles were counted). (D) HRTEM image highlighting the lattice fringes associated with the {121} plane of the  $\text{YFeO}_3$  orthorhombic phase.





**Fig. 4.** XPS spectra of the Y 3d, Fe 2p, O 1s orbitals for the NP and C-films. The Y 3d and O 1s spectra were deconvoluted, while interference from the Sn 3p<sub>3/2</sub> line in the Fe 2p region prevented a fully quantitative analysis. Both films exhibited a surface Y:Fe ratio of 70:30.

reflectance data do not provide fully conclusive evidences of the formation of YFeO<sub>3</sub>.

High resolution XPS spectra of both films in the regions of Y 3d, O 1s and Fe 2p are shown in Fig. 4. The Y 3d spectra contains contributions from Y 3d<sub>3/2</sub> and Y 3d<sub>5/2</sub> that can be deconvoluted in two further components. The main Y 3d<sub>5/2</sub> component at 156.5 eV (labelled as 1) is related to the formation of Y<sub>2</sub>O<sub>3</sub> [35,36] as a consequence of the Y surface segregation, whereas the component at 157.6 eV (peak 2) corresponds to Y<sup>3+</sup> in the perovskite lattice [37]. The atomic percentage of Y as Y<sub>2</sub>O<sub>3</sub> is 66.5% and 80% in the C and NP-film, suggesting a higher extent of A-site segregation at the surface of the NP-film. Four different components were considered in the deconvolution of the O 1s line (see Table S1 in the supporting information). The lower binding energy component at 529.1 eV is assigned to the oxygen in the perovskite lattice. The second component at 530.6 eV can be attributed to hydroxyl groups, whereas the third component at 531.8 eV is linked to carbonyl groups. The component with the highest binding energy is associated with adsorbed molecular water. For the NP-YFeO<sub>3</sub> sample, a strong contribution of SnO<sub>2</sub> from the FTO substrate was

observed. In this case, component 2 of the O 1s line also includes the contribution from SnO<sub>2</sub>.

The Fe 2p region of the photoemission spectrum (Fig. 4) provides further insights into the surface composition of the films. The Fe 2p<sub>3/2</sub> and Fe 2p<sub>1/2</sub> peaks are located at 710.2 eV and 724.4 eV, respectively, which are consistent with the presence of Fe<sup>3+</sup>. The satellite peak located at 718.4 eV further confirms this oxidation state. In the case of the NP-YFeO<sub>3</sub> sample, a new component at 715.9 eV is observed which can be linked to the Sn 3p from the FTO. Based on the contributions of the Fe 2p and Y 3d regions, the Y:Fe surface ratio can be estimated taking into account the corresponding sensitivity factors. An Y:Fe ratio of 70:30 is found for the C and NP-films, confirming a Y-surface enrichment in accordance with a previous report on perovskite oxides [38]. However, it is interesting that the analysis of the Y 3d region shows a larger content of the binary (Y<sub>2</sub>O<sub>3</sub>) oxide at the surface in the case of the NP-films, which are synthesized at significantly higher temperatures in comparison to C-films. This analysis suggests that, although XRD shows a remarkable degree of phase purity, the

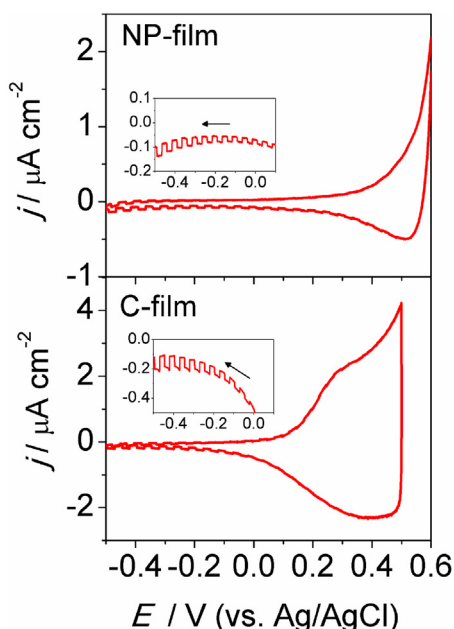


**Fig. 5.** Cyclic voltammetry at  $5 \text{ mV s}^{-1}$  under transient illumination (404 nm and photon flux of  $1.0 \cdot 10^{16} \text{ cm}^{-2} \text{ s}^{-1}$ ) of NP and C-films. Illumination was performed from the back side.

nanoparticle surface appears to contain a complex mixture of secondary oxide phases.

Fig. 5 displays the photoelectrochemical responses of the NP- and C-YFeO<sub>3</sub> electrodes under square-wave light perturbation at  $5 \text{ mV s}^{-1}$ . The voltammograms are characterized by a potential independent capacitive response at negative potentials and a large increase of the current towards more positive values. The NP-films show a substantial increase of the current at potentials above 0.4 V vs Ag/AgCl (1.35 V vs RHE), which is associated with hole accumulation at the interface. This behavior suggests that the potential associated with the valence band edge is located in this potential range. On the other hand, carrier accumulation can already be seen from 0.1 V in the case of C-films. This is also a manifestation of band tails arising from the amorphous nature of the material. Consequently, there is an effective density of states spreading from the valence band edge into the gap.

The photocurrent onset potential is located close to 0.1 V vs Ag/AgCl (1.05 V vs RHE) as seen in Fig. 5, as well as by experiments recorded under lock-in detection with a higher frequency of light perturbation (Supporting Information, Fig. S2). This onset potential is close to values reported for other ternary iron oxides, namely LaFeO<sub>3</sub>, CaFe<sub>2</sub>O<sub>4</sub>, CuFe<sub>2</sub>O<sub>4</sub> or CuFeO<sub>2</sub> [14,16,17,19,20]. Interestingly, the intensity and potential dependence of the photocurrent is similar for both films despite the large difference in crystallinity. Experiments were also carried out in contact with O<sub>2</sub> saturated solutions (see Supporting Information, Fig. S3). No substantial changes in the photocurrent were observed, although the NP-film showed larger dark currents at negative potentials. This behavior is associated with pin-holes in the NP-film, allowing oxygen reduction to take place at the FTO electrode (this is confirmed by a voltammetric analysis in the presence of oxygen at a bare FTO in Fig. S4).

Fig. 6 displays the photocurrent transients at different potentials for the NP- and C-YFeO<sub>3</sub> electrodes under back illumination. The overall photocurrent increases towards more negative potentials. NP-films exhibit a photocurrent decay after the initial response towards a photostationary current value, followed by a sharp decay to zero upon switching off the light. A

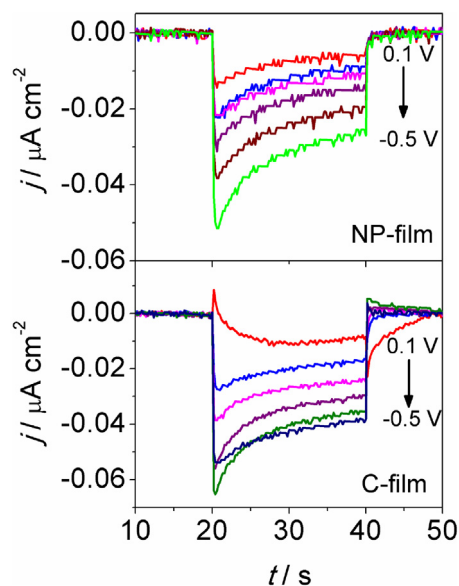


**Fig. 6.** Photocurrent transient responses under illumination at 404 nm and photon flux of  $1.0 \times 10^{16} \text{ cm}^{-2} \text{ s}^{-1}$  at different potentials for the NP and C-films. Electrolyte solution is Ar-saturated 0.1 M NaOH. Illumination was performed from the back side.

similar behavior is observed for the C-films, although a rather interesting feature is observed at 0.1 V. This transient exhibits a positive instantaneous photocurrent, a negative photostationary value and a negative photocurrent overshoot upon switching off illumination. Again, this response coincides with the onset of electron depopulation of tail states from the valence band observed in the voltammetric measurements (see Fig. 5). In contrast to the responses at more negative potentials, the transient at 0.1 V in the case of the C-film shows evidence of surface recombination [39,40]. Thus, spikes upon illumination and light interruption indicate electron trapping at the surface, promoting surface recombination. Furthermore, the decay observed on the second timescale can be described in terms of a redistribution of the potential drop across the film/electrolyte interface, leading to a time dependent recombination. This type of phenomena is observed in materials with low carrier mobility [41].

Fig. 7 shows the photostationary current after 20 s ( $j_{ss}$ ) as a function of photon flux under illumination through the back contact (back) and the semiconductor-electrolyte boundary (front). C-films show very similar photocurrent responses under back and front illumination, thus only the former is shown. The

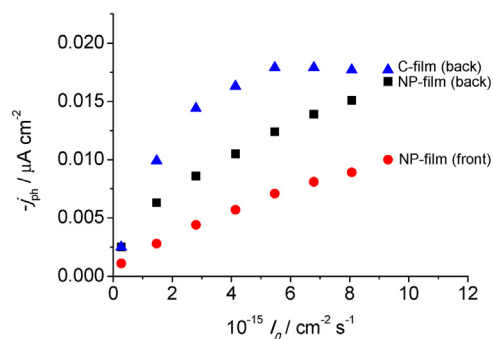


**Fig. 7.** Photostationary current ( $j_{ss}$ ) obtained for NP and C-films as a function of the photon flux. Measurements carried out under back and front illumination are shown in the case of NP-films. Only back illumination is shown for the C-film, as little difference was observed with respect to front back illumination. The experiments were performed under potentiostatic conditions at  $-0.5 \text{ V vs Ag/AgCl}$ .

photocurrent increases with photon flux in a rather non-linear relationship. This is a clear indication of a substantial carrier recombination, which also manifest itself by the rather low IPCE values (below 0.01%). Despite substantial differences in film thickness, surface roughness and crystallinity, the photocurrent magnitude and photon-flux dependence is comparable for NP and C-films. This behavior provides a clear indication that only carriers generated close to the back contact (FTO) are effectively collected at the back contact. This is supported by the fact that photocurrent responses are higher under back illumination in the case of NP-films, while not such a contrast is observed in the case of C-films due to the significantly lower film thickness (80 nm).

The low collection efficiency of carriers can be associated with two key factors, carrier recombination and hole-capture by water. As mentioned previously, the potential associated with the valence band edge is located at approximately 1.35 V vs RHE, which raises the possibility that the poor hole collection efficiency is due to hole capture by water to generate oxygen or hydrogen peroxide. This carrier loss mechanism appears consistent with the photocatalytic performance reported for  $\text{YFeO}_3$  [22–26]. On the other hand, recombination losses can be linked to A-site surface segregation as shown by our XPS measurements, leading to an insulating yttrium oxide layer irrespective of the calcination temperature. In the case of NP-films, this insulating layer will not only affect electron transfer to evolve hydrogen, but also interparticle carrier transport in the film. In the case of C-film, Y-segregation may have a weaker effect on the charge transport in the film. However, the presence of tail states due to the amorphous nature of the oxide will have a strong effect on carrier mobility. The fact that the photocurrent onset potential is close to the valence band edge reveals the suitability of  $\text{YFeO}_3$  as photocathode for hydrogen generation. It should be mentioned that IPCE values for hydrogen evolution under alkaline conditions are typically lower than in acid solutions [42], consequently, improvement in photoresponses will require optimized surface passivation and deposition of co-catalysts as recently reported for a variety of semiconductors [9,43–45].

#### 4. Conclusions

$\text{YFeO}_3$  thin films electrodes were prepared by two different methodologies, sintering of phase-pure nanoparticles (NP) and compact (C) films by sol-gel. The former was obtained after calcination of an ionic-liquid based precursor at 1000 °C, while the temperature of the C-film thermal treatment was limited to 640 °C. The NP-films were characterized by an orthorhombic perovskite structure with no secondary phases, while C-films were essentially amorphous. The high crystallinity of the NP films manifested itself by a sharp band gap transition at 2.45 eV and a clear onset potential for hole-extraction from the valence band edge located at 0.4 V vs  $\text{Ag}/\text{AgCl}$  (1.35 V vs RHE) estimated from cyclic voltammetry. On the other hand, the amorphous C-film exhibited a distribution of density of states tailing into the band gap region as probed by spectroscopic and electrochemical analysis. XPS indicates that +3 is the main Fe oxidation state present in both films. Despite the significant difference in crystallinity, XPS clearly shows that the surface of both films is Y-rich (70:30 Y:Fe atomic ratio) with a significant presence of binary Y oxide at the NP-films surface.

Photoelectrochemical studies in Ar-saturated 0.1 M NaOH solution were characterized by potential dependent responses with an onset potential close to 0.1 V vs  $\text{Ag}/\text{AgCl}$  (1.05 V vs RHE) in the absence of any catalysts. The photocurrent responses show complex dynamic features revealing hindered charge transport and bulk recombination. Evidence of surface recombination was observed in the C-films at potentials in which valence band tail states are partially depopulated. The photocurrent dependence on photon flux at 404 nm was highly non-linear, with rather low IPCE

values. We postulate that holes generated close to electrolyte junctions can be lost by the water oxidation itself, leading to a photochemical water-splitting event and low collection efficiency of majority carriers at the back contact.

#### Acknowledgements

VC gratefully acknowledges the Royal Society and the UK National Academy by the support through the Newton International Fellows program and EPSRC via the UK Catalysis Hub (EP/K014706/1 and EP014714/1). DT and DJF is grateful to EPSRC for funding through the PVTEAM Programme (EP/L017792/1), as well as to the Institute of Advanced Studies of the University of Bristol for the Research Fellowship. Electron microscopy studies were carried out both at the SSTTI of The University of Alicante and at the Chemical Imaging Facility of the University of Bristol with equipment partly funded by EPSRC (EP/K035746/1 and EP/M028216/1). MIDG is grateful to the Doctorate School of the University of Alicante for a travel grant. The Alicante team acknowledges the Spanish Ministry of Economy and Competitiveness for financial support through project MAT2015-71727-R (FONDOS FEDER).

#### Appendix A. Supplementary data

Supplementary data associated with this article can be found, in the online version, at <http://dx.doi.org/10.1016/j.electacta.2017.06.025>. Data are available at the University of Bristol data repository, data.bris, at <https://doi.org/10.5523/bris.2vm60z83uv9n02g2ll6tyvvszt>.

#### References

- [1] B.A. Pinaud, J.D. Benck, L.C. Seitz, A.J. Forman, Z. Chen, T.G. Deutsch, B.D. James, K.N. Baum, G.N. Baum, S. Ardo, H. Wang, E. Miller, T.F. Jaramillo, Technical and economic feasibility of centralized facilities for solar hydrogen production via photocatalysis and photoelectrochemistry, *Energy Environ. Sci.* 6 (2013) 1983–2002.
- [2] M.M. May, H.-J. Lewerenz, D. Lackner, F. Dimroth, T. Hannappel, Efficient direct solar-to-hydrogen conversion by in situ interface transformation of a tandem structure, *Nat. Commun.* 6 (2015) 8286.
- [3] V. Cristino, S. Caramori, R. Argazzi, L. Meda, G.L. Marra, C.A. Bignozzi, Efficient photoelectrochemical water splitting by anodically grown  $\text{WO}_3$  electrodes, *Langmuir* 27 (2011) 7276–7284.
- [4] M. Jankulovska, I. Barceló, T. Lana-Villarreal, R. Gómez, Improving the Photoelectrochemical Response of  $\text{TiO}_2$  Nanotubes upon Decoration with Quantum-Sized Anatase Nanowires, *J. Phys. Chem. C* 117 (2013) 4024–4031.
- [5] M. Tallarida, C. Das, D. Cibrev, K. Kukli, A. Tamm, M. Ritala, T. Lana-Villarreal, R. Gómez, M. Leskelä, D. Schmeisser, Modification of Hematite Electronic Properties with Trimethyl Aluminum to Enhance the Efficiency of Photoelectrodes, *J. Phys. Chem. Lett.* 5 (2014) 3582–3587.
- [6] J. Quiñero, T. Lana-Villarreal, R. Gómez, Improving the photoactivity of bismuth vanadate thin film photoanodes through doping and surface modification strategies, *Appl. Catal. B Environ.* 194 (2016) 141–149.
- [7] Y. Lin, C. Battaglia, M. Boccard, M. Hettick, Z. Yu, C. Ballif, J.W. Ager, A. Javey, Amorphous Si thin film based photocathodes with high photovoltage for efficient hydrogen production, *Nano Lett.* 13 (2013) 5615–5618.
- [8] R.H. Coridan, M. Shaner, C. Wiggenshorn, B.S. Brunschwig, N.S. Lewis, Electrical and Photoelectrochemical Properties of  $\text{WO}_3/\text{Si}$  Tandem Photoelectrodes, *J. Phys. Chem. C* 117 (2013) 6949–6957.
- [9] A. Paracchino, V. Laporte, K. Sivula, M. Grätzel, E. Thimsen, Highly active oxide photocathode for photoelectrochemical water reduction, *Nat. Mater.* 10 (2011) 456–461.
- [10] C.G. Morales-Guio, L. Liardet, M.T. Mayer, S.D. Tilley, M. Grätzel, X. Hu, Photoelectrochemical Hydrogen Production in Alkaline Solutions Using  $\text{Cu}_2\text{O}$  Coated with Earth-Abundant Hydrogen Evolution Catalysts, *Angew. Chemie Int. Ed.* 54 (2015) 664–667.
- [11] B. Kaiser, D. Fertig, J. Ziegler, J. Klett, S. Hoch, W. Jaegermann, Solar hydrogen generation with wide-band-gap semiconductors:  $\text{GaP}(100)$  photoelectrodes and surface modification, *ChemPhysChem* 13 (2012) 3053–3060.
- [12] K. Fujii, K. Kusakabe, K. Ohkawa, Photoelectrochemical properties of  $\text{InGaN}$  for  $\text{H}_2$  generation from aqueous water, *Jpn. J. Appl. Phys.* 44 (2005) 7433–7435.
- [13] Y. Matsumoto, K. Sugiyama, E.-I. Sato, Improvement of  $\text{CaFe}_2\text{O}_4$  photocathode by doping with Na and Mg, *J. Solid State Chem.* 74 (1988) 117–125.

- [14] J. Cao, T. Kako, P. Li, S. Ouyang, J. Ye, Fabrication of p-type  $\text{CaFe}_2\text{O}_4$  nanofilms for photoelectrochemical hydrogen generation, *Electrochim. Commun.* 13 (2011) 275–278.
- [15] M.I. Díez-García, R. Gómez, Investigating Water Splitting with  $\text{CaFe}_2\text{O}_4$  Photocathodes by Electrochemical Impedance Spectroscopy, *ACS Appl. Mater. Interfaces* 8 (2016) 21387–21397.
- [16] M.I. Díez-García, T. Lana-Villarreal, R. Gómez, Study of Copper Ferrite as a Novel Photocathode for Water Reduction: Improving Its Photoactivity by Electrochemical Pretreatment, *ChemSusChem* 9 (2016) 1504–1512.
- [17] M.S. Prévot, N. Guijarro, K. Sivula, Enhancing the Performance of a Robust Sol-Gel-Processed p-Type Delafossite  $\text{CuFeO}_2$  Photocathode for Solar Water Reduction, *ChemSusChem* 8 (2015) 1359–1367.
- [18] A.K. Díaz-García, T. Lana-Villarreal, R. Gómez, Sol-gel copper chromium delafossite thin films as stable oxide photocathodes for water splitting, *J. Mater. Chem. A* 3 (2015) 19683–19687.
- [19] V. Celorrio, K. Bradley, O.J. Weber, S.R. Hall, D.J. Fermin, Photoelectrochemical Properties of  $\text{LaFeO}_3$  Nanoparticles, *ChemElectroChem* 1 (2014) 1667–1671.
- [20] Q. Yu, X. Meng, T. Wang, P. Li, L. Liu, K. Chang, G. Liu, J. Ye, Highly Durable p- $\text{LaFeO}_3/\text{n-Fe}_2\text{O}_3$  Photocell for Effective Water Splitting under Visible Light, *Chem. Commun.* 51 (2015) 3630–3633.
- [21] M.I. Díez-García, R. Gómez, Metal Doping to Enhance the Photoelectrochemical Behavior of  $\text{LaFeO}_3$  Photocathodes, *ChemSusChem* 10 (2017) 2457–2463, doi:<http://dx.doi.org/10.1002/cssc.201700166>.
- [22] X. Lü, J. Xie, H. Shu, J. Liu, C. Yin, J. Lin, Microwave-assisted synthesis of nanocrystalline  $\text{YFeO}_3$  and study of its photoactivity, *Mater. Sci. Eng. B* 138 (2007) 289–292.
- [23] P. Tang, H. Chen, F. Cao, G. Pan, Magnetically recoverable and visible-light-driven nanocrystalline  $\text{YFeO}_3$  photocatalysts, *Catal. Sci. Technol.* 1 (2011) 1145–1148.
- [24] Y. Zhang, J. Yang, J. Xu, Q. Gao, Z. Hong, Controllable synthesis of hexagonal and orthorhombic  $\text{YFeO}_3$  and their visible-light photocatalytic activities, *Mater. Lett.* 81 (2012) 1–4.
- [25] Y. Chen, J. Yang, X. Wang, F. Feng, Y. Zhang, Y. Tang, Synthesis  $\text{YFeO}_3$  by salt-assisted solution combustion method and its photocatalytic activity, *J. Ceram. Soc. Japan* 122 (2014) 146–150.
- [26] M. Khraisheh, A. Khazndar, M.A. Al-Ghouti, Visible light-driven metal-oxide photocatalytic  $\text{CO}_2$  conversion, *Int. J. Energy Res.* 39 (2015) 1142–1152.
- [27] S. Geller, M.A. Gilleo, The crystal structure and ferrimagnetism of yttrium-iron garnet,  $\text{Y}_3\text{Fe}_2(\text{FeO}_4)_3$ , *J. Phys. Chem. Solids* 3 (1957) 30–36.
- [28] V. Cherepanov, I. Kolokolov, V. L'vov, The saga of YIG: Spectra, thermodynamics, interaction and relaxation of magnons in a complex magnet, *Phys. Rep.* 229 (1993) 81–144.
- [29] A. Navrotsky, Thermochemistry of complex perovskites, *AIP Conf. Proc.* (2000) 288–296.
- [30] J. Cheng, A. Navrotsky, X.-D. Zhou, H.U. Anderson, Enthalpies of Formation of  $\text{LaMO}_3$  Perovskites ( $\text{M} = \text{Cr}, \text{Fe}, \text{Co}, \text{and Ni}$ ), *J. Mater. Res.* 20 (2005) 191–200.
- [31] V. Celorrio, E. Dann, L. Calvillo, D.J. Morgan, S.R. Hall, D.J. Fermin, Oxygen Reduction at Carbon-Supported Lanthanides: The Role of the B-Site, *ChemElectroChem* 3 (2016) 283–291.
- [32] W. Wang, S. Li, Y. Wen, M. Gong, L. Zhang, Y. Yao, Y. Chen, Synthesis and Characterization of  $\text{TiO}_2/\text{YFeO}_3$  and Its Photocatalytic Oxidation of Gaseous Benzene, *Acta Physico-Chimica Sin.* 24 (2008) 1761–1766.
- [33] A. Skumanich, A. Fropa, N.M. Amer, Urbach tail and gap states in hydrogenated a-SiC and a-SiGe alloys, *Solid State Commun.* 54 (1985) 597–601.
- [34] A.R. Zanatta, I. Chambouleyron, Absorption edge, band tails, and disorder of amorphous semiconductors, *Phys. Rev. B* 53 (1996) 3833–3836.
- [35] P. de Rouffignac, J.-S. Park, R.G. Gordon, Atomic Layer Deposition of  $\text{Y}_2\text{O}_3$  Thin Films from Yttrium Tris( $\text{N,N}'$ -diisopropylacetamidate) and Water, *Chem. Mater.* 17 (2005) 4808–4814.
- [36] L. Wu, J.C. Yu, L. Zhang, X. Wang, S. Li, Selective self-propagating combustion synthesis of hexagonal and orthorhombic nanocrystalline yttrium iron oxide, *J. Solid State Chem.* 177 (2004) 3666–3674.
- [37] J. Li, U.G. Singh, T.D. Schladt, J.K. Stalick, S.L. Scott, R. Seshadri, Hexagonal  $\text{YFe}_{1-x}\text{Pd}_x\text{O}_{3-\delta}$ : Nonperovskite host compounds for  $\text{Pd}^{2+}$  and their catalytic activity for CO oxidation, *Chem. Mater.* 20 (2008) 6567–6576.
- [38] J. Druce, H. Tézé, M. Burriel, M.D. Sharp, L.J. Fawcett, S.N. Cook, D.S. McPhail, T. Ishihara, H.H. Brongersma, J.A. Kilner, Surface termination and subsurface restructuring of perovskite-based solid oxide electrode materials, *Energy Environ. Sci.* 7 (2014) 3593–3599.
- [39] L.M. Peter, Dynamic aspects of semiconductor photoelectrochemistry, *Chem. Rev.* 90 (1990) 753–769.
- [40] J. Li, R. Peat, L.M. Peter, Surface recombination at semiconductor electrodes. Part II. Photoinduced near-surface recombination centres in p-GaP, *J. Electroanal. Chem.* 165 (1984) 41–59.
- [41] A. Gomis-Berenguer, V. Celorrio, J. Iniesta, D.J. Fermin, C.O. Ania, Nanoporous carbon/ $\text{WO}_3$  anodes for an enhanced water photooxidation, *Carbon* 108 (2016) 471–479.
- [42] J.O. Bockris, K. Uosaki, Rate of the photoelectrochemical generation of hydrogen at p-type semiconductors, *J. Electrochem. Soc.* 124 (1977) 1348–1355.
- [43] S. Hu, N.S. Lewis, J.W. Ager, J. Yang, J.R. McKone, N.C. Strandwitz, Thin-Film Materials for the Protection of Semiconducting Photoelectrodes in Solar-Fuel Generators, *J. Phys. Chem. C* 119 (2015) 24201–24228.
- [44] C.-Y. Lin, Y.-H. Lai, D. Mersch, E. Reisner,  $\text{Cu}_2\text{O}/\text{NiO}_x$  nanocomposite as an inexpensive photocathode in photoelectrochemical water splitting, *Chem. Sci.* 3 (2012) 3482–3487.
- [45] S. Chen, S.S. Thind, A. Chen, Nanostructured materials for water splitting – State of the art and future needs: A mini-review, *Electrochim. Commun.* 63 (2016) 10–17.